Time-Resolved Absorptance and Melt Pool Dynamics during Intense Laser Irradiation of a Metal

Brian J. Simonds,[*] Jeffrey Sowards,[†] Josh Hadler, Erik Pfeif,[‡] Boris Wilthan, Jack Tanner, Chandler Harris, Paul Williams, and John Lehman

National Institute of Standards and Technology, 325 Broadway, Boulder, Colorado 80305, USA

(Received 2 April 2018; revised manuscript received 2 July 2018; published 25 October 2018)

High-irradiance lasers incident on metal surfaces create a complex, dynamic process through which the metal can rapidly change from highly reflective to strongly absorbing. Absolute knowledge of this process underpins important industrial laser processes such as laser welding, cutting, and metal additive manufacturing. Determining the time-dependent absorptance of the laser light by a material is important, not only for gaining a fundamental understanding of the light-matter interaction but also for improving process design in manufacturing. Measurements of the dynamic optical absorptance are notoriously difficult due to the rapidly changing nature of the absorbing medium. These data are also of vital importance to process modelers, whose complex simulations need reliable, accurate input data; yet, there are very few available. In this work, we measure the time-dependent, reflected light during a 10-ms laser spot weld using an integrating-sphere apparatus. From this, we calculate the dynamic absorptance for 1070-nm-wavelength light incident on 316L stainless steel. The time resolution of our experiment (less than 1 μs) allows the determination of the precise conditions under which several important physical phenomena occur, such as melt and keyhole formation. The average absorptances determined optically are compared with calorimetrically determined values, and it is found that the calorimeter severely underestimates the absorbed energy due to mass lost during the spot weld. Weld-nugget cross sections are also presented to verify our interpretation of the optical results, as well as to provide experimental data for weld-model validation.

DOI: 10.1103/PhysRevApplied.10.044061

I. INTRODUCTION

The recent accessibility of high-power laser systems has greatly increased their range of practical applications, in particular for manufacturing. What was once useful only in niche applications has now become an important industrial tool, in large part due to greatly reduced cost and operational complexity. These systems are highly sought by industry for processes such as laser welding, cutting, and additive manufacturing for the benefits of increased productivity, faster weld speeds, design flexibility, and reduced capital expenditures. However, the availability of industrial high-power laser systems has outpaced the knowledge of how the high-irradiance beams they produce interact with a metal target. This interaction is complicated by the fact that the high-power laser beams are dynamically changing the target surface over a large temperature range and through multiple phase changes. Therefore, the quantification of a basic property such as absorptance, which determines energy coupling and thereby underpins the predictions of any laser-matter interaction simulation, is incredibly difficult. Because of a lack of precise knowledge of the dynamic energy coupling at high irradiance levels, energy absorptance is typically treated as a tuning parameter for mathematical models. The goal of this work is to provide high-accuracy input and output data allowing modelers to validate the physics of their simulations and to elucidate physical phenomena such as melting and keyhole formation with absolute, dynamic absorptance measurements.

In this paper, we study the interaction of high-irradiance laser light on a solid metal target, which is most analogous to laser welding. It also provides a suitable stepping stone for understanding the related, but much-more-complicated, systems found in additive manufacturing where light is incident on a metal powder. Laser-welding simulations have been under development for decades to improve weld procedures and to gain a better understanding of the joining process. These are complex computer models that solve differential equations typically for heat transport, material mechanics, fluid flow, and vapor dynamics to predict metallurgical effects. The long-range vision of these simulations is to eliminate the time and money associated with empirical process development such that a qualified

[*]brian.simonds@nist.gov

[†]Currently at NASA Marshall Space Flight Center, Huntsville, Alabama 35812, USA

[‡]Currently at Johns Manville, 10100 West Ute Avenue, Littleton, Colorado 80127, USA

weld can be produced the first time it is attempted—in other words, that they are predictive. At present, however, there are several roadblocks that limit the utility of these simulations in real-world process development.

Currently, a model is empirically "calibrated" to select the appropriate input parameters that yield agreement with measured results [1]. Common inputs for laser-weld models include thermophysical, mechanical, and optical property data of the base material over a wide range of phases and temperatures. Ideally, a laser-weld modeler would be able to find accurate property data in the literature for the material of interest. In practice, however, the published literature will, at best, provide a starting point for model calibration, which is even less true for new or exotic alloys that have not been extensively studied. Even in the case of well-established materials, acceptable composition tolerances within a particular alloy class can lead to drastically different properties. As just one example, thermophysical properties of austenitic stainless steels have been found to differ drastically in the literature: surface tension due to sulfur [2,3] and oxygen [3] content; thermal diffusivity [4] and linear expansion coefficient [5] due to Fe:Cr:Ni ratios. Values for optical properties such as reflectance, emittance, and absorptance can differ even more widely as they are dependent on surface roughness and sample preparation [6–8]. In addition, the values used for model inputs are results culled from numerous different laboratories, with research spanning several decades, using different experimental techniques on materials from different feedstocks, which, in turn, result in increased ambiguity for the modeled system. As a result, the model calibration procedure requires its own time-intensive, iterative loop parallel to that needed for empirical process development. As the available parameter space created by the range of process parameters is quite large, one could argue that less-robust models could be tuned to give acceptable results while missing important physics of the internal weld process. This is an obvious hindrance to the goal of using such models to reliably predict results such as thermal history and weld microstructure.

The ideal approach to this problem is to provide a source of high-accuracy experimental input and output data that can be used to confirm a model's prediction. Toward this goal, we provide the measured dynamic coupling efficiency during a single spot weld under well-known, albeit simple boundary conditions. This is a critical input parameter for laser-weld modeling, for which there are scant data in the literature. Cross-section images of the weld nuggets are provided as a measured output against which a model can be validated.

The material used was a National Institute of Standards and Technology (NIST) Standard Reference Material (SRM) for 316L stainless steel [9]. As a SRM, the composition is maintained and certified by NIST and is available for public purchase, which allows further material properties to be obtained as model demands require and as experimental techniques improve. While many aspects of the experiments performed here exist in the literature, the novelty of this work is that it ties well-characterized optical measurements and weld results to a standard material in a single resource. In addition, determining accurate uncertainties is a vital part of this work as these determine the range of acceptable outcomes for weld simulations. As a complete data set, this work can be used to validate the underpinning physics and calculations of a simulation. Once achieved, this validated simulation can be used with more confidence to predict results for a more-complicated material system for which the modeler provides thermophysical property data.

Previous measurements of optical coupling efficiency can be generalized into two categories: those that give an average value and those that measure the coupling dynamically (i.e., as a function of time). The former has typically used a calorimetry-based approach where the temperature rise of the sample is measured and related to the total heat input from the laser [10–13]. Measurements of dynamic coupling have been conducted by a few researchers who used an integrating sphere to capture the light scattered during a laser weld [14–17]. We take a similar approach as the nature of the process is highly dynamic with rapidly changing coupling. Also, it does not require alteration of the sample by attachment of probes, does not rely on knowledge of a heat capacity (thus introducing additional uncertainties), and can be integrated to give an absorbed-energy result as in calorimetry-based methods. With regard to this latter point, we measure the average coupling efficiencies using a dynamic approach and compare the results with those we obtain from calorimetry measurements, and find that during keyhole welding, the calorimeter measurements require an energy correction term due to mass loss, which introduces additional assumptions and uncertainty. Furthermore, the time-resolved data in this work reveal several physical phenomena during the laser-welding process not encapsulated in a single, calorimetry-based average coupling value. These include the solid-liquid phase change, the onset of keyhole formation and its instability, and hydrodynamic behavior of the molten weld pool.

This paper is organized as follows. A thorough description of the material, experimental procedures, and analytical methods used is provided first. The cross-section dimensions and images of the weld are given for a range of energy densities resulting in conduction through keyhole welds. Next, dynamic light scattering results are presented along with the dynamic absorptance determined. These are then compared with calorimetry-based measurements performed under nominally identical conditions. Last, a thorough discussion is presented on the phenomena revealed in the dynamic data.

TABLE I. Chemical composition of NIST SRM 1155a [9].

Element	Fe	Cr	Ni	Mo	Mn	Si
Mass	$(64.71 \pm 0.12)\%$	$(17.803 \pm 0.099)\%$	$(12.471 \pm 0.056)\%$	$(2.188 \pm 0.015)\%$	$(1.593 \pm 0.060)\%$	$(0.521 \pm 0.017)\%$
Element	Cu	Co	W	V	P	C
Mass	$(0.2431 \pm 0.0050)\%$	$(0.225 \pm 0.018)\%$	$(0.0809 \pm 0.0059)\%$	$(0.0725 \pm 0.0046)\%$	$(0.0271 \pm 0.0012)\%$	$(0.0260 \pm 0.0036)\%$
Element	Nb	Ti	N	As	Sn	S
Mass	$(0.0082 \pm 0.0014)\%$	$(0.0039 \pm 0.0012)\%$	$(0.0482 \pm 0.0024)\%$	$(0.007 \pm 0.003)\%$	$(0.0069 \pm 0.0013)\%$	$(0.0020 \pm 0.0009)\%$

II. MATERIALS AND METHODS

A. Sample preparation

For these experiments, we use NIST SRM 1155a [9], which is a 316L stainless steel with the composition listed in Table I. Samples are precisely cut into discs 11 mm in diameter and 2 mm thick with a mass of $1.464 \pm .020$ g. They are then polished with 240-grit sandpaper to remove large-scale features, followed by wet sanding with 2400- and 4000-grit sandpaper for 30 s each to give a mirrorlike finish. Surface-roughness measurements of five identically prepared samples show an average root-mean-square roughness of 79 ± 20 nm. Figure 1, which shows optical profilometry data [Fig. 1(a)] and an optical image [Fig. 1(b)] of a representative sample, reveals that the polishing procedure leaves some micrometer-scale scratches on the surface. The sample surfaces are cleaned with acetone and blown dry with compressed gas before a laser spot weld.

The use of a SRM is important in this work for several reasons. First, it is a feedstock of material whose composition has been verified and will remain the same for all samples within the stated measurement tolerances. Thermophysical properties, in particular thermal diffusivity [18], can vary as a function of composition even within the tolerances defined for a particular alloy class. Therefore, by using a SRM for these measurements, we can assume that the thermophysical properties vary negligibly from sample to sample. Furthermore, any future thermophysical data collected for this particular SRM (1155a) can be referenced to the data in this paper for the purposes of modeling. Thus, as measurement techniques improve for difficult-to-measure properties, such as surface tension and viscosity of the melt, if they are performed on this SRM, the data presented here will still be relevant.

B. Weld cross sections

Weld-nugget dimensions are obtained by our cross-sectioning samples mounted and polished in phenolic resin. The weld centers are found by our progressively polishing samples toward the center with 240–800-grit SiC paper. To develop a contrast between the weld nugget and the base metal, the specimens are etched with aqua regia ($3HCl{:}1HNO_3$). Images are obtained with an optical stereoscope. Cross-section widths are compared with the premounted, top-down widths, and the polishing process is repeated until the two numbers agree to within 4%. It is found that the image plane of maximum width sometimes differs from the image plane at which the maximum weld depth occurs. The spatial difference between these two image planes is on the order of 10 μm, and the difference in weld depth between these two planes is less than 6% in all instances. The cross-section images shown in this work are those at the plane of maximum weld width. However, all reported values for weld width or weld depth are the maximal values measured at any plane. Additional polishing and etching beyond these planes gives weld-nugget dimensions that become smaller, which ensures that the numbers reported here are at the maximums to within the uncertainty reported. Uncertainty due to repeatability is estimated from cross sections of six

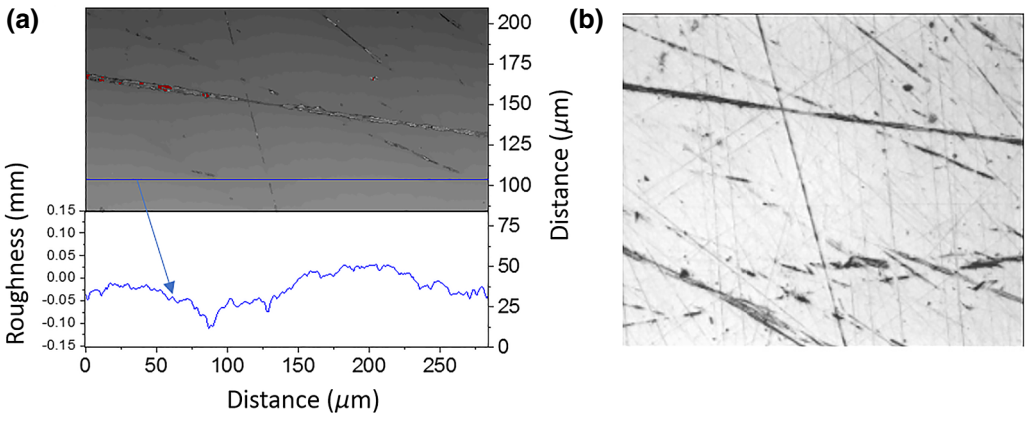

FIG. 1. (a) Optical profilometry data and cross section of a sample representative of that used in this study. (b) Optical microscope image of same location as used in (a).

nominally-identically-prepared samples. This results in a standard deviation in width and depth of 7% and 4%, respectively.

C. Dynamic absorptance measurements

The general arrangement of the dynamic measurement is shown in Fig. 2(a). Laser spot welding is performed with a commercial fiber laser operating at 1070 nm with 10-ms illumination. The temporal profile of the laser output is roughly square with a rise time of about 10 μs. Laser light is delivered to a commercial laser weld head by a 100-μm-diameter, multimode fiber focused with a 150-mm-focal-length lens. This produces a top-hat spot at the focal plane that is 303 μm in diameter as measured by its full width at the $1/e^2$ value [see Fig. 2(c)]. The output energy is measured with a commercial power meter with a stated uncertainty of 3% before the sample is put in place.

An integrating sphere is used to capture the off-normal-axis scattered light from the weld pool. The sphere is three-dimensionally printed from a dark-colored plastic in two halves as shown in Fig. 2(b). When combined, they have an outer diameter of 75 mm and an inner diameter of 65 mm; the light entrance port is 7.5 mm in diameter. The target sample is placed on the opposite side of the sphere, which has an aperture of 5 mm. The inner surface is coated with a $BaSO_4$ paint, which creates a diffuse surface after the application of several (approximately 20) thin layers. This coating is similar to that used in the work reported in Ref. [19] and is particularly convenient for our purposes as imperfections caused by weld spatter could simply be painted over. A baffle is incorporated into the sphere design to ensure that neither the weld pool nor the plume is directly visible to the detection optics on the sphere wall [see Fig. 2(b)].

Two photodiodes are used to detect the scattered light during the laser spot welds: one is attached to the laser weld head, and the other is fiber-coupled to the wall of the integrating sphere. Both are adjustable-gain InGaAs photodiodes with 1070-nm-bandpass filters preceding them. The first is used to detect light scattered directly back into the weld head at normal incidence. This photodiode has a neutral-density filter (optical density 2) and a rise time (based on the manufacturer's specification and its gain setting) of 21 ns. The second photodiode detects light from the integrating sphere and that is passed through a 1070-nm-bandpass filter. A second attenuation filter is used during the spot weld, which has transmission at 1070 nm of $0.089 \pm 1\%$. Its gain setting corresponds to a response time of 450 ns.

For each measurement, normal incidence of the laser light is confirmed from the back reflection of a low-power guide beam coincident with the weld-laser beam. The exact energy applied during a single spot weld is determined by our averaging ten pulses fired immediately before the spot weld is performed. The average standard deviation of these

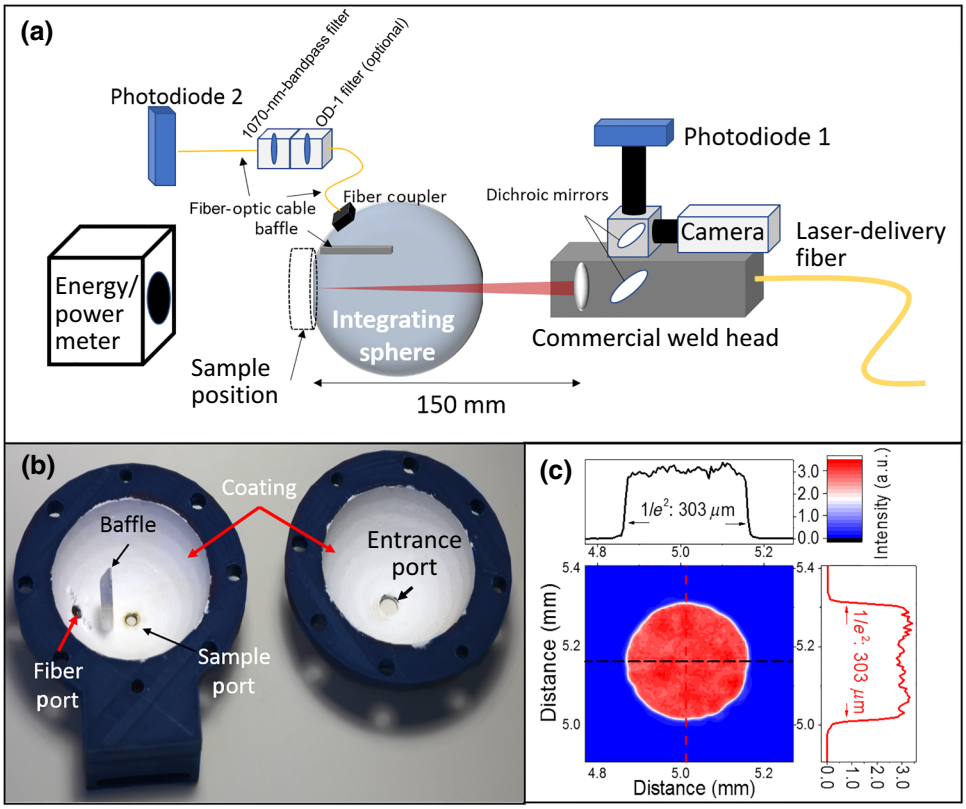

FIG. 2. (a) The experimental setup of the optical measurements. (b) The inside halves of the three-dimensionally-printed integrating sphere with white $BaSO_4$ coating. (c) The measured beam profile at the focal point of the laser beam used. OD, optical density.

pulses is 0.4%. This process also allows us to determine the amount of ambient light scattered within the weld held in the absence of a sample, which is subtracted from the weld-head photodiode signal.

The measurement procedure for obtaining dynamic absorptance data is as follows. First, the weld-head photodiode is calibrated by our calculating the normal-incidence reflected light from an optical-quality, fused quartz sample by subtracting the transmitted energy from the initial input energy. These values are determined by successive application of ten 10-ms pulses with use of a commercial energy meter and the assumption of negligibly small absorption at 1070 nm in the quartz sample. This is performed over a range of input energies to determine a calibration constant, C_{head} with unit of watts per millivolt, by a weighted linear fit. It is assumed that the calibration of the weld-head photodiode is valid between successive spot-weld measurements. Therefore, the absolute scattered power detected in the weld head, P_{head}, is determined from the raw weld-head photodiode signal, S_{head} (mV), according to

$$P_{\text{head}} = C_{\text{head}} S_{\text{head}}. \tag{1}$$

A value for a single standard uncertainty in P_{head} is determined through general propagation of errors [20]. The uncertainty in the calibration factor is determined by our adding in quadrature the systematic errors resulting from the precisions of our oscilloscope (1%) and laser energy meter (3%) with the random errors determined from the deviation to the best linear fit. The random errors are minimized by our averaging ten values for each data point in the fit. The result is a 3.7% standard uncertainty (confidence interval of 68%) in P_{head}.

The integrating-sphere photodiode is calibrated separately before each spot weld as weld spatter could slightly alter the sphere's inner surface in successive runs. It is calibrated with a gold, diffuse scattering target in place of the sample in Fig. 2(a). A description of the preparation of the target sample and its measured bidirectional reflectance-distribution function and reflectance losses can be found in Ref. [21]. A correction of 0.978 is applied to the measured signal to account for the losses due to sample absorption and losses through the sphere entrance port. Because of the damage-threshold limitation of this target, much-lower energy densities are used for the calibration. To ensure that the signal range of our detection system covers the range that is typical during the laser spot weld, the attenuation filter is removed during the calibration. In a similar manner to the weld-head photodiode, a calibration parameter C_{sphere} is measured, and the absolute power P_{sphere} is determined from

$$P_{\text{sphere}} = C_{\text{sphere}} \left(\frac{S_{\text{sphere}}}{T} \right). \tag{2}$$

The additional term T is the transmission of the 1070-nm-bandpass filter. Since the value of C_{sphere} is determined before each spot weld, the standard uncertainty values of P_{sphere} varies slightly, but remained between 3.5% and 4.0%.

The absorbed power, $P_{\text{abs}}(t)$, is found by our subtracting the total light lost during the weld from the input power as

$$P_{\text{abs}}(t) = P_0(t) - [P_{\text{head}}(t) + P_{\text{sphere}}(t)]. \tag{3}$$

The functional form of the time dependence of P_0 is determined from a measurement of the backscattered light from the quartz sample during the weld-head photodiode calibration. It is normalized such that the integral of P_0 equals the measured laser energy. Therefore, its uncertainty is the manufacturer's specification of the energy meter, or 3%. Normalization of $P_{\text{abs}}(t)$ by P_0 (t) gives the dynamic absorptance, $A(t)$, during the spot weld:

$$A(t) = \frac{P_{\text{abs}}(t)}{P_0(t)}. \tag{4}$$

The total energy absorbed, E_{abs}, during the spot weld is determined from the time integral of the absorbed power.

$$E_{\text{abs}} = \int P_{\text{abs}}(t)dt = \int [P_0(t) - P_{\text{head}}(t) - P_{\text{sphere}}(t)]dt. \tag{5}$$

If one assumes that the three components on the right-hand side of Eq. (5) are independent, then our adding their uncertainties in quadrature gives the total uncertainty in P_{abs}, and therefore E_{abs}. An additional component of uncertainty is added in quadrature for the repeatability of the measurement of E_{abs}. This is determined from the standard deviation of five repeated measurements. The average coupling efficiency during the entire spot weld can be calculated according to

$$\eta_{\text{coupling}} = \frac{E_{\text{abs}}}{E_0}, \tag{6}$$

with its uncertainty found by general propagation of errors.

D. Calorimetry

Calorimetry is used in an effort to validate the values of total absorbed energy obtained from the optical measurements. The calorimeter is made of commercially available polystyrene, whose low thermal conductivity [22] makes it suitable for calorimetry. The sample rests in the base, which is approximately $5 \times 10 \times 10$ cm^3. A 1-cm-thick polystyrene cover containing a 6-mm aperture is placed over the sample for a total calorimeter thickness of approximately 6 cm [see Fig. 3(a)]. The sample surface is placed at the focus of the weld laser. The temperature rise of the sample is measured by two type-N thermocouples with leads 254 μm in diameter that are welded to the

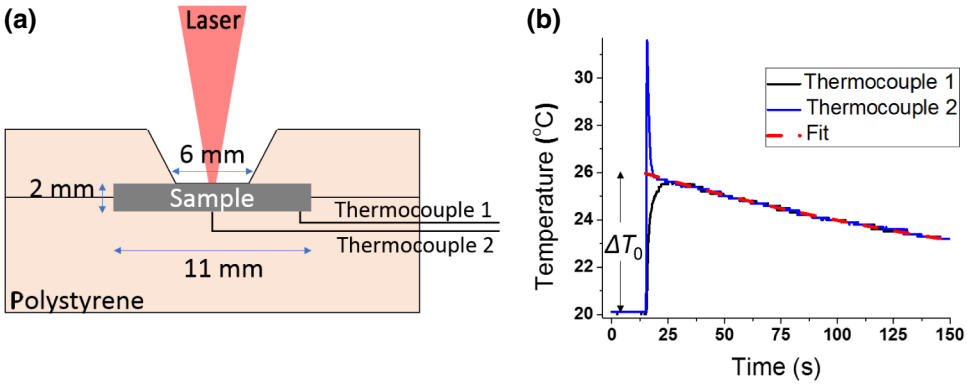

FIG. 3. Calorimeter design (a) and representative data (b).

center and edge of the sample's rear surface. Representative thermocouple data are shown in Fig. 3(b). The energy collected by the calorimeter is calculated according to

$$E_0 = m\, C_p\, \Delta T_0, \tag{7}$$

where m is the puck mass and C_p is the specific heat. The room-temperature heat capacity of 316L stainless steel (0.50 J/g K) [23] is used as the temperature rise is only moderately above room temperature. Thermal-transport simulations (not shown here) show that the point where the sample comes into contact with the polystyrene cover is never more than 14 °C above room temperature and thus does not damage the calorimeter.

For our calorimeter, as well as similar devices [11,13,24], thermal losses are primarily from the front surface on which the laser light is incident. To account for these losses, the time regime where the values of the two thermocouples agree is fit to an exponential decay curve, from which the initial temperature rise (ΔT_0) when the laser is fired is calculated [see Fig. 3(b)]. This method, however, corrects only for those energy losses that are occurring when sample has reached equilibrium (about 5 s after the laser pulse). We consider two additional forms of energy loss that occur at much shorter times: (1) mass ejection during the spot weld and (2) radiative losses from the keyhole during the laser pulse. It is found that these losses are quite significant, in particular during keyhole welding. Additionally, we calculate the radiative losses from the entire exposed surface between the time the laser is off and the time when the sample has equilibrated, and find that they are not greater than 0.5% of E_0, and are therefore considered negligible.

Radiation and mass losses result only in a reduction of the total energy absorbed and therefore necessitate an energy-correction term be added to the calorimetry result. We estimate the energy lost from mass ejection according to

$$E_{\text{vapor/liquid}} = m[C_{p,s}\,\Delta T_1 + C_{p,l}\,\Delta T_2 + (H_m + H_v)T]. \tag{8}$$

The parameters are listed and defined in Table II. The first term accounts for the energy needed to melt solid stainless steel and depends on the difference in temperature between room temperature and the melting point, $\Delta T_1 = T_{\text{melt}} - T_{\text{room}}$. The next term describes the energy from heating the molten metal and the difference in temperature from the melting point to the vaporization temperature, $\Delta T_2 = T_{\text{vapor}} - T_{\text{melt}}$. The final terms result from the phase changes to liquid and gas and the corresponding enthalpies of melting and vaporization, H_m and H_v. The mass lost during a single weld is measured with a precision scale with 100-ng readability by our making ten identical spot welds each on a fresh spot of a single sample and determining the average mass difference per shot. The use of Eq. (8) necessitates the presumption of the phase of the ejected mass: whether it is from ejected metal droplets or is in vapor form. As it is most likely that there is a combination of both, we consider the two extreme cases of all liquid droplets and all vapor as lower and upper bounds to the energy-correction term. In the case of all liquid droplets, the H_v term is omitted from the calculation.

Next we consider the radiative energy lost from the weld pool region during the laser weld. This is determined by our integrating the rate of energy radiated, $P_{\text{radiative}}$, from a surface during a 10-ms (t_{pulse}) weld:

$$P_{\text{radiative}} = \frac{E_{\text{radiative}}}{t_{\text{pulse}}} = \varepsilon\,\sigma\, T_{\text{weld}}^4 A, \tag{9}$$

where σ is the Stefan-Boltzmann constant and A is the surface area of the weld nugget defined by the measured weld diameter, d_{weld}. We approximate the infrared emissivity of the weld area, ϵ, during the weld as the average

TABLE II. Parameters used for calorimetry energy-correction terms.

Parameter	Symbol	Value	Reference
Specific heat, solid	$C_{p,s}$	0.50 J/g K	[23]
Specific heat, liquid	$C_{p,l}$	0.79 J/g K	[23]
Enthalpy of melting	H_m	260 J/g	[23]
Enthalpy of vaporization	H_v	6360 J/g	[25,26]
Melting temperature	T_{melt}	1658 K	[23]
Vaporization temperature	T_{vapor}	3300 K	[25,26]

coupling efficiency, as this value represents an effective absorptivity over the duration of the spot weld. The temperature of the weld pool, T_{weld}, must also be known, but is notoriously difficult to measure. Therefore, we are forced to make reasonable estimates based on literature values. We are aided in this by the work of Tan *et al.* [25], who simulated pulsed-laser spot welds under very similar experimental conditions. In this work, their "case 5" is roughly the same energy density as our $E_{in} = 3.46$ J. Therefore, we use their predicted temperature of 3600 K for $E_{in} = 3.46$ J and make a range of reasonable estimates for T at higher and lower values of E_{in}.

III. RESULTS AND DISCUSSION

A. Weld cross section

Cross-section images of the spot welds are shown in Fig. 4 with increasing input energy (E_{in}), and are grouped in columns according to their appearance as conduction, transition, or keyhole welds. The lowest E_{in} (plots *a–c*) clearly produces welds that are indicative of conduction welding (shallow, broad weld nuggets). Increased E_{in} above about 3.5 J gives higher-aspect-ratio weld nuggets with fluted profiles that indicate keyhole welding (plots *d–f*). Intermediate weld nuggets share features of both, and are labeled as "transition" welds. There is some subjectivity with respect to the exact classification of these welds; however, our optical measurements make the distinction clearer. The measured weld-nugget width (W_{weld}) and length (L_{weld}) are given in Fig. 5(a). The uncertainty in the width and length is the standard deviation of six separate spot welds performed at $E_{in} = 3.3$ J. As the laser pulse energy is increased, the weld depth and diameter increase, with a small inflection in the transition region from conduction to keyhole welds. Other studies of laser spot welding show similar increasing trends but do not report an inflection [10,11,24]. The resolution of our data is undoubtedly increased as compared with these previous

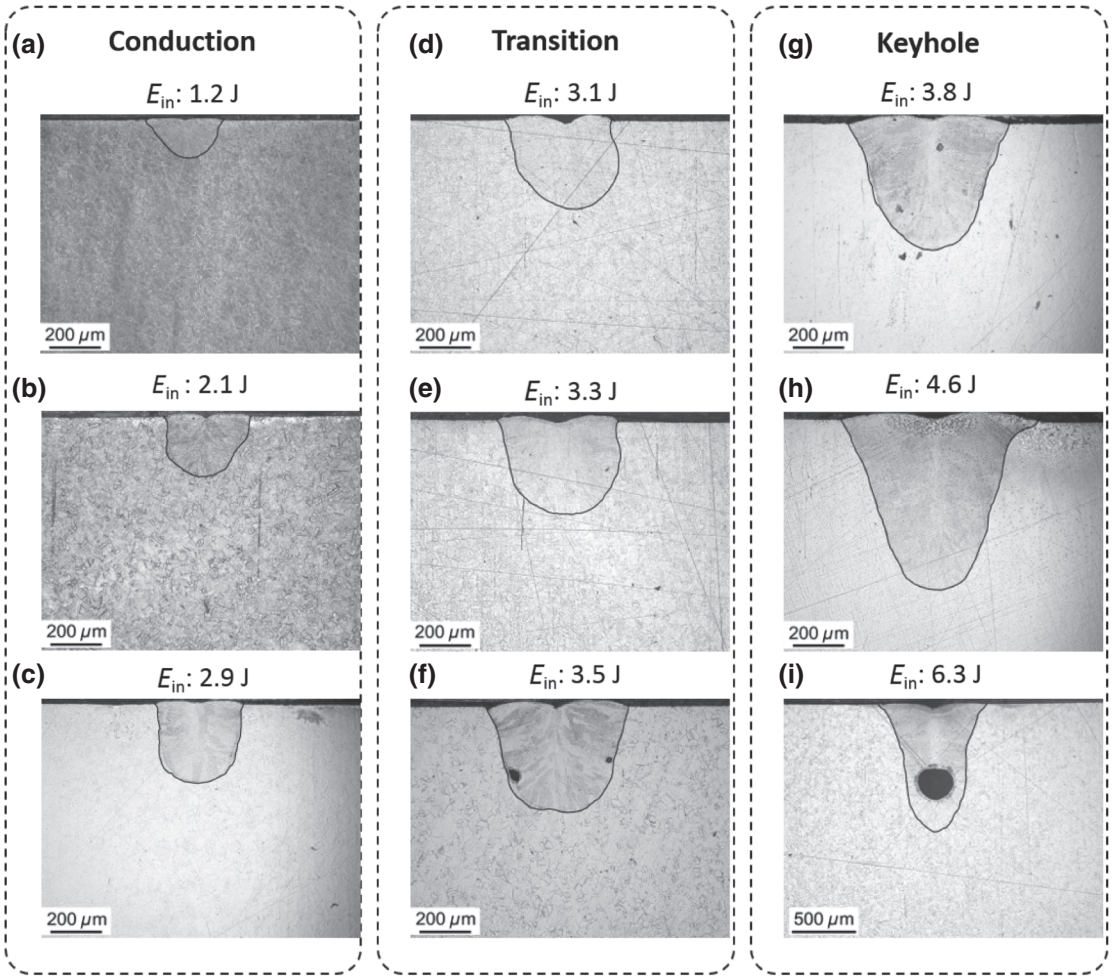

FIG. 4. Laser-weld cross sections for 10-ms spot welds at the labeled input energy, E_{in}. They are grouped according to their appearance as conduction, transition, or keyhole welds. Weld-nugget outlines are traced with a dark line to improve visibility. Note that all have the same length scale, except for plot *i*, which is 2.5 times larger.

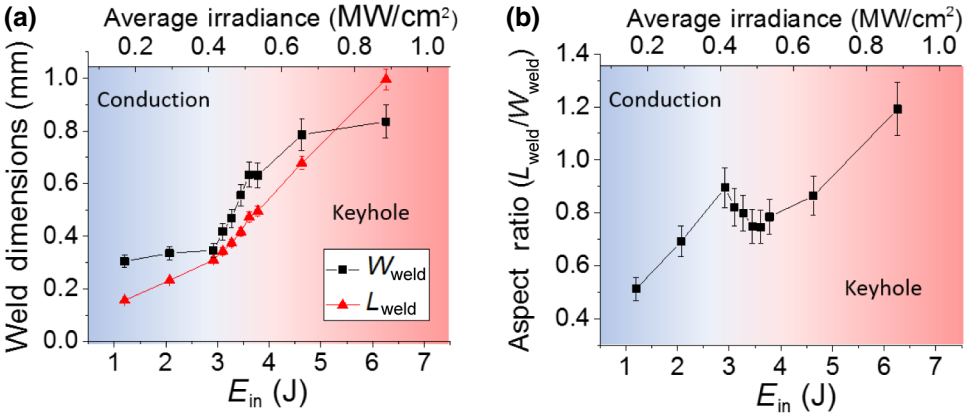

FIG. 5. (a) Laser-spot-weld nugget depth and diameter as a function of input energy, E_{in} (see also Table III for values) (b) The aspect ratio (L_{weld}/W_{weld}) of the weld nuggets as a function of input energy.

attempts due to the increased stability of our fiber laser source as opposed to the Nd:YAG sources used those previous attempts. This feature can more readily be seen in the aspect ratio (L_{weld}/W_{weld}) as shown in Fig. 5(b). The flattening of the aspect ratio is a sign of the transition from conduction and keyhole welds, which was observed previously [27].

B. Dynamic absorptivity during laser spot welding

Figure 6 shows the dynamic reflectance data from both photodiodes [$P_{sphere}(t)$ and $P_{head}(t)$; red and blue curves, respectively], as well as the power applied to the sample as a function of time [$P_0(t)$, black curves]. These data have been calibrated to represent the absolute values for power. The plots are organized according to their weld cross section and coupling efficiency (discussed below) as conduction (plots *a–c*), transition (plots *d–f*), or keyhole (plots *g–i*).

The data in Fig. 6 show that, overall, very little light is returned to the weld head during spot welding and contributes to the total scattered light only at early times. This is consistent with a transition of the weld target from a mostly specular solid surface to a volatile molten pool [16]. It is also clear that as the input energy is increased, this peak narrows, which is expected from more rapid melting. Therefore, at all but the lowest input energy, the absorptance calculation is almost entirely determined from light scattered within the integrating sphere.

The curves in Fig. 6 are used to perform an energy-balance calculation and compute the time-dependent absorptance with use of Eqs. (3) and (4). This is plotted in Fig. 7, which is organized from top to bottom in increasing E_{in}. There are several features in the absorptance data presented in Fig. 7 that are worth discussing. Starting at short times below 1 ms, all data show a steep rise, eventually followed by a decay. At low energy input, this happens at 600 μs and decreases rapidly as the energy input is increased. The sharpness of the feature suggests a dramatic change in the material properties such as the change that would accompany a phase change. This feature can be readily explained as a result of melting with the following logic. The initial rise is due to solid-state heating, which has been observed and credited to a variety of reasons. First, a rise in absorptivity with temperature is expected from a free-electron Drude model. However, the simplicity of the Drude theory considers only a perfectly flat surface. Observations of laser heating of steels under this condition show modest increases of absorptivity from about 0.09 to 0.12 over a temperature range of approximately 1000 °C from room temperature [28,29]. Oxide formation with heating has also been shown to increase absorptivity [30]. Kwon *et al.* [7] attributed the doubling of absorptance (from 30% to 60%) during submelting laser heating at 1.06 μm of 304 stainless steel to oxidation. Lastly, Wang *et al.* [6] saw a similarly dramatic increase in absorptivity with surface temperature, which they ascribed to a semisolid subphase characterized by a spontaneous surface roughening.

The subsequent drop in absorptance can be explained by the surface-roughness difference between the solid surface, which although polished is not optically flat, and a molten-metal pool. Surface roughness has been shown experimentally to increase the absorptivity in steel alloys in the solid under a wide range of surface treatments [6,8,28,30]. Therefore, on melting, the surface tension of the liquid metal removes the small amount of roughness and presents a specular surface to the incoming laser beam. This effect can easily be seen in plot *a* in Fig. 6, where an increase in the weld-head signal around 700 μs is concurrent with a decrease in the sphere signal, resulting in an overall decrease in absorptance in plot *a* in Fig. 7. This explanation is counter to the expectation of a Drude model, which predicts a small step-function increase in absorptivity at the melting point due to an increase in the number of free carriers [31]. However, on the basis of our interpretation, we believe that the effect is surface roughness dominated and is therefore not considered in a Drude model. There is insufficient research in the literature on the effects of changes in surface oxidation at the melting point on laser

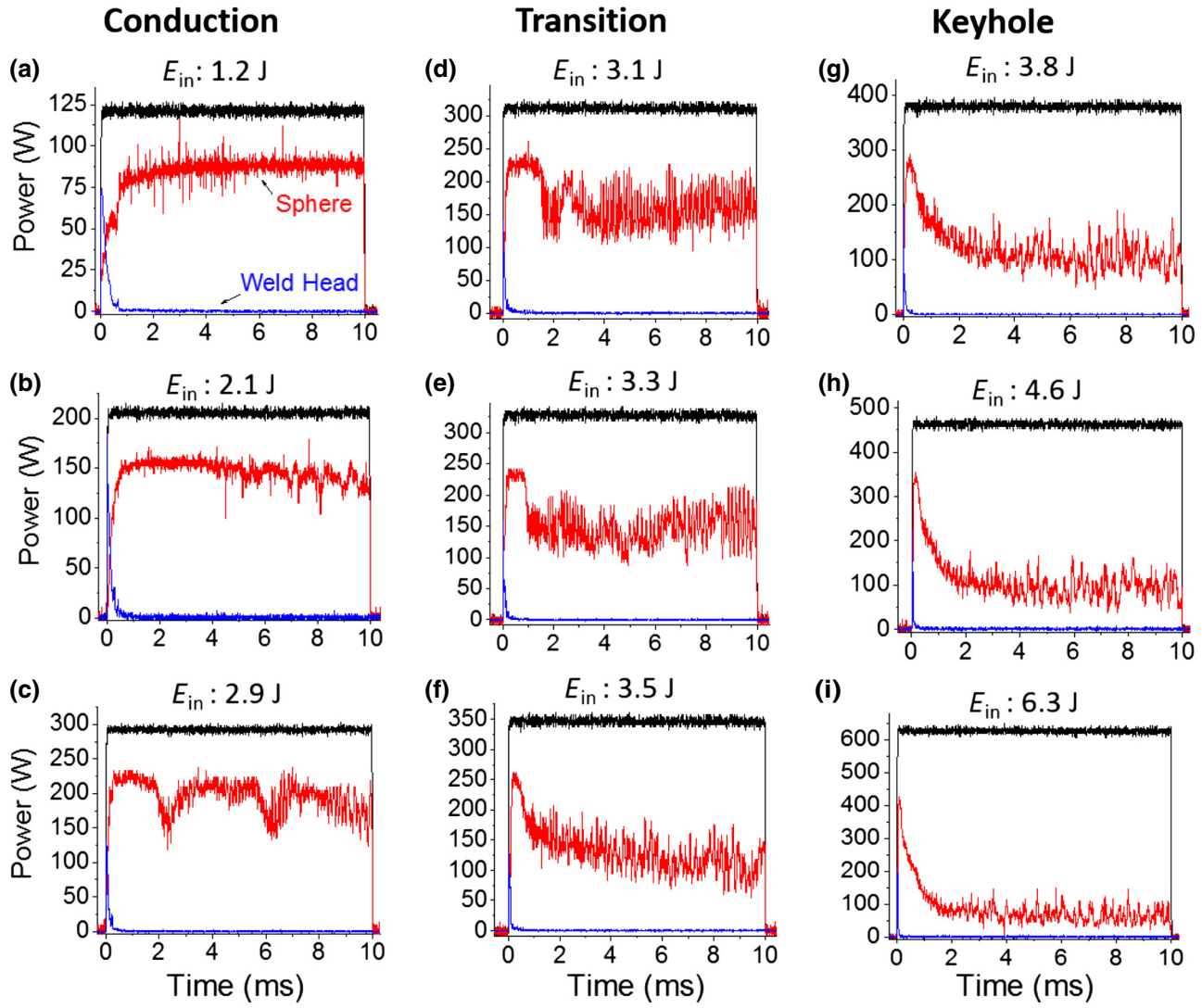

FIG. 6. Scattered light results showing the light scattered in both the weld head (P_{head}, blue) and the integrating sphere (P_{sphere}, red) as compared with the power input (P_0, black).

absorption, but it seems reasonable to believe that this could also contribute along with surface roughness to the effects seen here.

The next feature visible in plots *c*–*j* in Fig. 7 is a second rise in absorptance. As this feature occurs only in the materials where a keyhole geometry is seen in the cross-section images, it seems reasonable to believe that this rise in absorptance results from multiple scattering due to keyhole formation. Especially telling is the fact that plots *c* and *d* in Fig. 7, for which the data are taken just at the onset of keyhole formation, show multiple absorptance "humps" that indicate that one is on the cusp of forming a stable keyhole. A threshold for stable keyhole formation as a function of absorbed laser power has been predicted theoretically with oscillations in and out of a keyhole near the onset [32]. This assertion is also supported by the position of these data points in Fig. 10 (discussed later) as they are at the start of the sharp transition region.

With both of these features, one can define characteristic times described as time-to-melt [Fig. 8(a)] and time-to-keyhole [Fig. 8(b)] (see also Table III for values). The former is defined by the initial peak in absorptance. The latter we define as the time where the absorptance reaches 0.40, excepting the initial steep rise. This value is chosen as it lies on the rising edge of the feature that we ascribe to keyhole formation. By integrating $P_{abs}(t)$ from time zero to the time-to-keyhole, one can calculate the amount of absorbed energy necessary for keyhole formation. This is also shown in Fig. 8(b), as the energy-to-keyhole. The same general trend exists for both in that the time to establish either is dramatically shortened with increasing pulse energy.

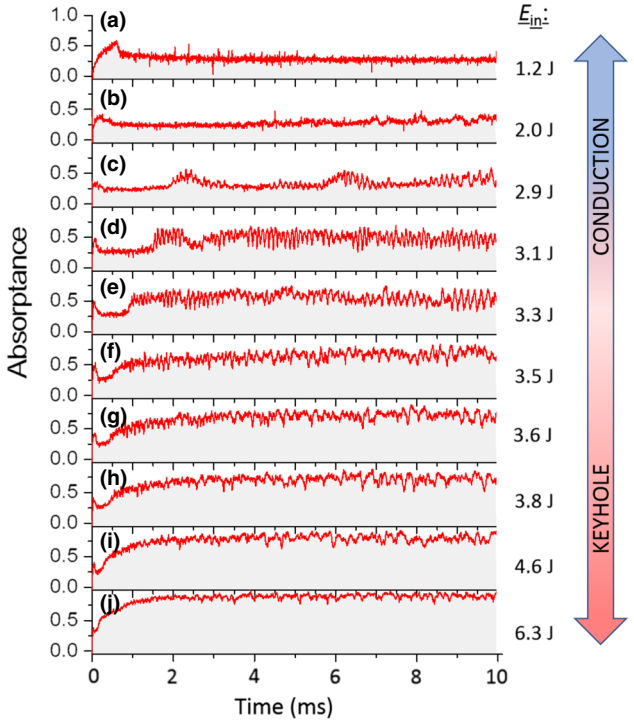

FIG. 7. Dynamic absorptance data found from Eq. (4). The ratio of the shaded region to the unshaded region in each graph is equal to the average coupling efficiency during the entire spot weld.

The time-to-keyhole presented in Fig. 8(b) shows an asymptotic behavior at higher energy. Fundamentally, it is expected that there be a lower limit to the time that it takes for keyhole formation as it is determined by the thermal transport properties, vaporization rates, and thermophysical properties of the material. A direct comparison with literature values for the time-to-keyhole is difficult given the dependence of the results on specific experimental parameters (spot size, laser power distribution, materials, etc.). However, the order of magnitude we observe is confirmed by several modeling studies of keyhole formation [25,26,33–35]. Keyhole modeling of spot welding in 304 stainless steel with comparable parameters by Tan *et al.* [25] calculated rapid keyhole growth on the order of milliseconds with tapering effects at 10 ms. Modeling of Nd:YAG spot welding by Zhou *et al.* [26] shows keyhole formation by 6 ms, but with a 1-ms power ramp, which would delay this compared with our experiments. Lastly, a model for laser spot welding by Courtois *et al.* [33] shows keyhole formation times ranging from to 8 ms over the range of parameters calculated. Experimentally, Matsunawa *et al.* [36] with high-speed imaging of aluminum spot welding showed a time-to-melt of 200 μs and a time-to-keyhole of 1 ms. Clearly these results support the general results we observe; however, future work will focus on gaining supporting evidence specific to our exact experimental arrangement.

The final feature of note in Fig. 7 is the high-frequency, periodic oscillations that begin to appear in plot *c* in Fig. 7 (2.9 J) and are most intense in plot *d* in Fig. 7 (3.1 J) and plot *e* in Fig. 7 (3.3 J). These appear after the time-to-melt and only in those samples that eventually exhibit keyhole behavior. To further understand this behavior, the frequency components of these curves are calculated by a fast Fourier transform over the temporal region where they exist. These are plotted in Fig. 9 on the same scale for easy comparison for curves in the conduction region (plot *a*), transition region (plots *b* and *c*), and keyhole region (plot *d*). In the frequency range from 0 to 15 kHz, the conduction result (plot *a*) shows no discernable feature. In the transition region, strong frequency components appear between 7 and 10 kHz, shifting from higher to lower values as the pulse energy is increased slightly. In keyhole mode (plot *d*), the frequency components are much lower, in the few-kilohertz regime.

Periodic oscillations associated with laser keyhole welding have been studied extensively over the past 30 years. An exact, quantitative comparison with literature results is difficult as they depend strongly on specific experimental conditions. A qualitative discussion is given here, with a more-detailed analysis the subject of future work. Experimental evidence of oscillatory behavior has been seen from high-speed imaging [36–38], plume-emission studies [39–42], acoustic emissions [40,43,44], and scattered probe beams [37,45]. For laser welding near 1-μm wavelengths, where the plasma is not strongly absorbed by the plume, these oscillations are believed to be from mechanical oscillations of the molten metal. The frequency of oscillations typically observed is below 10 kHz but can differ widely depending on laser power [43], weld speed [40,42,43], spot size [39], shield gas flow [42], etc. These oscillations have been shown to correlate with weld penetration depth, and could therefore be used for *in situ* weld monitoring of weld quality [41,42,44]. Significant computational efforts have gone into calculating the oscillatory-mode eigenfrequencies of the keyhole in radial, axial, and azimuthal directions [32,39,40,46], which result from instabilities around a balance of pressures that wish to push the keyhole open (ablation and gas flow) and those that wish to close it (surface tension, hydrostatic pressure, and fluid flow). These calculations generally agree with observations of oscillations below 10 kHz.

An interpretation of our data that is consistent with these previous results is as follows. The oscillations seen under keyhole-formation conditions (plot *d* in Fig. 9) appear to be most likely from keyhole dynamics of the type described and calculated by Klein *et al.* [32,39] to be in the 1–4-kHz regime. This has been verified experimentally by several groups [38–40,42–45]. These oscillations have a shorter wavelength and are less intense than those appearing at the onset of the transition region (plots *c*–*e* in Fig. 7 and plots *b* and *c* in Fig. 9). An explanation for these

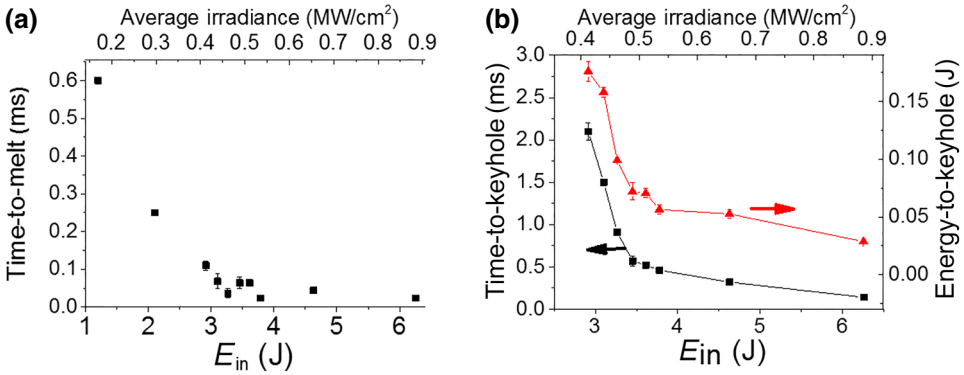

FIG. 8. The amount of time for the onset of melting (a) and the formation of a keyhole (b) as a function of laser pulse energy.

oscillations, as well as the trend toward lower frequency over a very-narrow-input-energy range, can be taken from Semak *et al.* [37], who calculated the eigenfrequencies of a melt pool not yet in keyhole mode. They did so for two different regimes: (1) for surface capillary waves (drumhead oscillations) where the melt pool depth is smaller than the radius and (2) for volumetric oscillations where the depth is larger than the radius. The frequency of the latter was found to be 2–3 times less than the frequency of the capillary waves as more molten mass is now oscillating. Therefore, the strong, high-frequency oscillations at the onset of the transition region (plot *b* in Fig. 9) are due to instability-induced surface waves resulting, most likely, from the initiation of surface vaporization.

A functional form for the natural frequency of capillary weld pool oscillations during gas-tungsten-arc welding is given by Xiao and den Ouden [47] and depends only on surface tension, the density of the molten metal, and the weld diameter. Using values of 0.9 N/m for the surface tension in the presence of oxygen [23], 6900 kg/m^3 for the density of molten stainless steel [48], and the measured diameters from Fig. 4, we find the values given by the vertical arrows in plots *b* and *c* in Fig. 9. The decrease in the intensity of these oscillations coincides with the deepening of the keyhole seen in Fig. 4. This is a result as our absorption measurement being more sensitive to physical oscillations of the molten pool when it is in the plane of the original metal surface (as in conduction-mode welding), which is why they are readily visible in plots *c*–*e* in Fig. 7. Our optical signal would be less sensitive to the axial, radial, and azimuthal oscillations that occur with a keyhole [32]. It is worth noting that although no fluctuations are seen in plot *a* in Fig. 9 in the range presented, there are two relatively weak (around 1 kW) spectral components at 18 and 28 kHz, which is consistent with our interpretation of a small, relatively placid melt pool at low energies. Although these results suggest that our interpretation is plausible, we caution that further work is necessary to more-definitely ascertain the exact nature and mode of these oscillations.

C. Average coupling efficiency from optical and calorimeter data

The integral of the total absorbed power versus time is equal to the total amount of energy absorbed during the spot weld. From Eqs. (4)–(6), this is proportional to the integrated area under the curves in Fig. 7. The average weld coupling efficiency from optical data is plotted in Fig. 10 as black squares. It is also given, along with other quantitative values from the integrating-sphere measurements, in Table III. At low values of E_{in}, the coupling efficiency remains roughly constant at around 30%. A steep increase is seen after $E_{in} = 2.9$ J, when the efficiency

TABLE III. Optical results from integrating-sphere measurements. Physical weld parameters of width (W_{weld}) and length (L_{weld}) are given, as well as the total absorbed energy (E_{abs}) and the average coupling efficiency ($\eta_{coupling}$).

E_{in} (J)	Average irradiance (MW/cm^2)	W_{weld} (μm)	L_{weld} (μm)	E_{abs} (J)	$\eta_{coupling}$	Time-to-melt (ms)	Time-to-keyhole (ms)
1.2	0.170	304	156	0.378	0.31	0.60	–
2.05	0.290	335	232	0.640	0.31	0.25	–
2.92	0.412	346	310	1.020	0.35	0.11	2.1
3.10	0.439	418	343	1.550	0.50	0.068	1.5
3.27	0.462	468	374	1.794	0.55	0.036	0.91
3.45	0.489	556	417	2.209	0.64	0.064	0.57
3.61	0.511	633	472	2.535	0.70	0.064	0.52
3.78	0.535	631	495	2.620	0.69	0.024	0.46
4.63	0.655	786	679	3.580	0.77	0.044	0.32
6.26	0.889	836	996	5.370	0.86	0.024	0.14

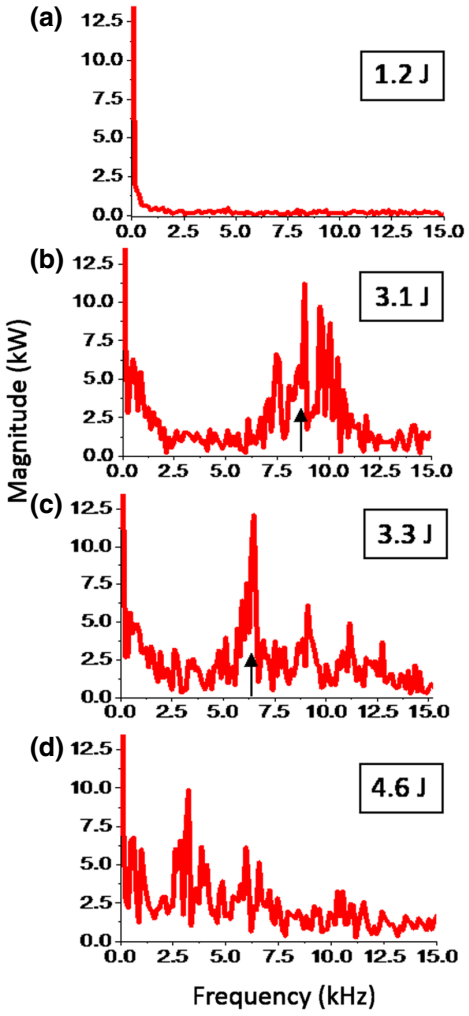

FIG. 9. Frequency spectra of select dynamic absorptance data obtained by fast Fourier transform. The vertical arrows in plots *b* and *c* give the calculated frequency of vibration of a melt pool as described in the text.

is less than 35%, which by $E_{\text{in}} = 3.8$ J has nearly doubled. At higher values of E_{in}, the efficiency continues to increase, to nearly 90% for the highest value measured. This observation is consistent with observations of many others who have seen a sharp increase in absorptance due to keyhole formation and the multiple reflections it allows [10,12,13,24]. Therefore, the sharp increase of efficiency can be ascribed as a transition from conduction to keyhole welding. This interpretation is consistent with the observations of the weld-nugget cross sections in Fig. 4.

Calorimetry is used to validate the optical results as the final temperature rise resulting from the spot weld should correspond to the total absorbed energy through Eq. (7). This is also useful as it allows comparison with similar experiments from the literature [11–13]. The coupling efficiency from calorimetry is simply the ratio of the absorbed energy (E_0) calculated from Eq. (7) to E_{in}. These results are plotted alongside the sphere results in Fig. 10, with the uncorrected data given by the dashed line and corrected values as stars. Two data points for each E_{in} are necessary to represent the upper and lower bounds for these losses as discussed previously. The uncertainties in these points reflect the standard uncertainties of the calorimeter measurement and not those of the assumptions for the corrections. Table IV shows the measured temperature differences from calorimetry (ΔT_0) and the absorbed energy, E_0, calculated from Eq. (7).

From Fig. 10, at $E_{\text{in}} = 2.91$ J (i.e., when in conduction mode), the calorimetry value is slightly larger than the sphere value. However, the low value of ΔT_0 (1.69 K) has a relatively high uncertainty such that the two values agree within a 95% confidence interval. As E_{in} increases, the uncorrected average efficiency values from calorimetry begin to strongly deviate outside the range explained by experimental uncertainty (dashed red curve in Fig. 10). This difference is accounted for by the energy losses not measured by the calorimeter; namely, losses from vaporization, weld spatter, and radiation that we have attempted to quantify. The measured mass lost from each sample for a single spot weld is given Table IV, which is used in Eq. (8) to determine E_{vapor} and E_{liquid} in Table IV. The radiative losses from the keyhole are determined from Eq. (9) with use of W_{weld} and ϵ, which are also listed in Table IV. Equation (9) requires that the temperature of the weld pool, T_{weld}, be known. As discussed previously, this was estimated from Tan *et al.* [25], with our estimates given in Table IV along with the radiative-energy correction term, $E_{\text{radiative}}$.

The rightmost columns in Table IV give lower and upper bounds for the total energy lost, E_{lost}. The lower bound

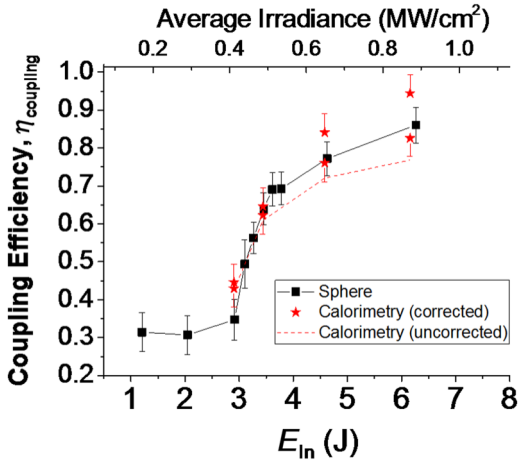

FIG. 10. Average coupling efficiency, η_{coupling}, during a single, 10-ms laser spot weld as determined from optical data (black squares). The red stars represent upper and lower bounds of the coupling efficiency as measured by calorimetry and corrected for mass loss. The error bars are the standard uncertainty of the measurement. The dashed line shows the uncorrected calorimetry data.

TABLE IV. Results from calorimetry including energy-correction terms for calorimeter results. See Eqs. (7)–(9) for the definition of the terms.

E_{in} (J)	ΔT_0 (K) Lower bound	E_0 (J) Upper bound	Mass loss (μg)	Emissivity, ϵ	E_{vapor} (J)	E_{liquid} (J)	T_{weld} (K)	$E_{radiative}$ (J)	Total E_{lost} (J)	
2.91	1.69	1.23	5.8	0.35	0.0485	0.0116	3300	0.0026	0.014	0.062
3.44	2.87	2.10	12.6	0.64	0.1053	0.0252	3600	0.0122	0.047	0.127
4.58	4.52	3.30	58	0.77	0.4848	0.1160	4000	0.0513	0.183	0.552
6.16	6.48	4.73	115	0.86	0.9613	0.2299	4500	0.1052	0.355	1.087

assumes that all of the mass lost is in liquid form and the upper bound assumes it is in vapor form; both include $E_{radiative}$. These terms become the extremes of the correction values applied to our raw calorimetry data (red stars in Fig. 10). The range of these bounds encompasses the integrating-sphere result. At higher values of E_{in}, when keyhole formation is observed, E_{lost} can be a significant fraction of the energy absorbed: a 23% correction to E_0 for the highest E_{in} used in this work. Additionally, the magnitude of this correction relies on assumptions about the temperature and optical properties of the keyhole, as well as the phase of the mass ejected. The uncertainty in these parameters leads to a very large ambiguity in the actual absorbed energy as measured by calorimetry. Since the magnitude of the correction increases with the size of the keyhole, we consider the average coupling-efficiency values from the integrating sphere to be much more robust as it does not suffer from these shortcomings. Other researchers have suspected as much [11,13], but until now a comparison with another technique has not been made. Nevertheless, we find good agreement between the optical results and those from calorimetry once the necessary corrections are made. However, we note that the corrections can be significant, especially during keyhole welding, and that the uncertainty involved with those corrections can render the results less reliable. Furthermore, our correction analysis does not consider unabsorbed light that is lost through scattering from ejected material. This scattered light would be collected and accounted for with the integrating-sphere approach, but would further add to E_{lost} in the calorimetry measurement. Quantifying this loss is beyond the scope of this work.

IV. CONCLUSION

We measure the dynamic absorptance during laser spot welding of 316L stainless steel NIST SRM with sub-1-μs time resolution. As a function of laser energy, we unambiguously identify key features such as the time at which melting occurs and the keyhole forms. A sharp transition in the average coupling efficiency marks the transition from conduction-mode welding to keyhole welding. This is confirmed with cross-section images of the laser weld nuggets. We associate with these measurements a rigorous uncertainty of energy absorption and laser irradiance. Furthermore, we compare the value of the average coupling efficiency obtained optically with that from calorimetry. We find that the absorbed energy determined from calorimetry is severely underestimated due primarily to mass ejection during keyhole spot welding. We also observe temporal features during the weld evolution that may give us access to melt pool physics relying on viscosity and molten-metal density.

ACKNOWLEDGMENTS

The authors are extremely grateful to Professor Stephen Liu and Professor Wei Zhang for valuable discussions and insight. Matt Spidell is appreciated for his careful reading and analysis of the manuscript. We also thank Cheryl Hawk for assistance with preparing the weld cross sections. This work of the U.S. Government is not subject to U.S. copyright.

[1] L. E. Lindgren, Numerical modelling of welding, Comput. Methods Appl. Mech. Eng. **195**, 6710 (2006).
[2] Z. Li, K. Mukai, M. Zeze, and K. Mills, Determination of the surface tension of liquid stainless steel, J. Mater. Sci. **40**, 2191 (2005).
[3] B. Ribic, P. Burgardt, and T. DebRoy, Optical emission spectroscopy of metal vapor dominated laser-arc hybrid welding plasma, J. Appl. Phys. **109**, 83301 (2011).
[4] Y. S. Touloukian and C. Y. Ho, *Thermophysical Properties of Matter* (IFI/Plenum, New York, 1970), Vol. 4.
[5] P. D. Desai, Thermodynamic properties of iron and silicon, J. Phys. Chem. Ref. Data **15**, 967 (1986).
[6] J. Wang, C. Weng, J. Chang, and C. Hwang, The influence of temperature and surface conditions on surface absorptivity in laser surface treatment, J. Appl. Phys. **87**, 3245 (2000).
[7] H. Kwon, W. K. Baek, M. S. Kim, W. S. Shin, and J. J. Yoh, Temperature-dependent absorptance of painted aluminum, stainless steel 304, and titanium for 1.07 μm and 10.6 μm laser beams, Opt. Lasers Eng. **50**, 114 (2012).
[8] D. Bergström, J. Powell, and A. F. H. Kaplan, The absorptance of steels to Nd:YLF and Nd:YAG laser light at room temperature, Appl. Surf. Sci. **253**, 5017 (2007).
[9] SRM 1155a., *AISI 316 Stainless Steel* (National Institute of Standards and Technology; U.S. Department of Commerce, Gaithersburg, MD, 2013).

[10] P. W. Fuerschbach, Measurement and Prediction of Efficiency in Laser Beam Energy Transfer Welding, Weld. J. **75**, 24s (1996).
[11] P. W. Fuerschbach and G. R. Eisler, Effect of laser spot weld energy and duration on melting and absorption, Sci. Technol. Weld. Join. **7**, 241 (2002).
[12] O. Perret, P. Naudy, and M. Bizouard, in *ICALEO '99 Laser Mater. Process. Conf.* (1999), pp. 177–186.
[13] J. Trapp, A. M. Rubenchik, G. Guss, and M. J. Matthews, In situ absorptivity measurements of metallic powders during laser powder-bed fusion additive manufacturing, Appl. Mater. Today **9**, 341 (2017).
[14] C. Sainte-Catherine, M. Jeandin, D. Kechemair, J.-P. Ricaud, and L. Sabatier, Study of dynamic absorptivity at 10.6 μm (CO2) and 1.06 μm (Nd-YAG) wavelengths as a function of temperature, J. Phys. IV **1**, C7-151–C7-157 (1991).
[15] R. Fabbro, S. Slimani, F. Coste, and F. Briand, Study of keyhole behaviour for full penetration Nd–Yag CW laser welding, J. Phys. D. Appl. Phys. **38**, 1881 (2005).
[16] J. T. Norris, C. V. Robino, M. J. Perricone, and D. A. Hirschfeld, Development of a time-resolved energy absorption measurement technique for laser beam spot welds, Weld. J. **89**, 75 (2010).
[17] C. Robino, Engineering approximations in welding: Bridging the gap between speculation and simulation, Weld. J. **95**, 1 (2016).
[18] Y. S. Touloukian, R. W. Powell, C. Y. Ho, and M. C. Nicolaou, *Thermophysical Properties of Matter, Vol. 10 Thermal Diffusivity* (IFI/Plenum, New York, 1973).
[19] F. Grum and G. W. Luckey, Optical sphere paint and a working standard of reflectance, Appl. Opt. **7**, 2289 (1968).
[20] J. R. Taylor, *An Introduction to Error Analysis* (University Science Books, 1997), 2nd ed.
[21] J. Zeng and L. Hanssen, in *Proc. SPIE 7453, Infrared Spaceborne Remote Sens. Instrum. XVII* (2009), pp. 1–10.
[22] E. Mihlayanlar, Ş Dilmaç, and A. Güner, Analysis of the effect of production process parameters and density of expanded polystyrene insulation boards on mechanical properties and thermal conductivity, Mater. Des. **29**, 344 (2008).
[23] K. C. Mills, *Recommended Values of Thermophysical Properties for Selected Commercial Alloys* (Woodhead Publishing Ltd., Cambridge, England, 2002).
[24] D. A. Cremers, G. K. Lewis, and D. R. Korzekwa, Measurement of energy deposition during pulsed laser welding, Weld. J. **70**, 159s (1991).
[25] W. Tan, S. B. Neil, and C. S. Yung, Investigation of keyhole plume and molten pool based on a three-dimensional dynamic model with sharp interface formulation, J. Phys. D. Appl. Phys. **46**, 55501 (2013).
[26] J. Zhou, H.-L. Tsai, and P.-C. Wang, Transport phenomena and keyhole dynamics during pulsed laser welding, Trans. Am. Soc. Mech. Eng. **128**, 680 (2006).
[27] A. M. Chelladurai, K. A. Gopal, S. Murugan, S. Venugopal, and T. Jayakumar, Energy transfer modes in pulsed laser seam welding, Mater. Manuf. Process. **30**, 162 (2015).
[28] T. J. Wieting and J. L. Derosa, Effects of surface condition on the infrared absorptivity of 304 stainless steel, J. Appl. Phys. **50**, 1071 (1979).
[29] S. Boyden and Y. Zhang, Temperature and wavelength-dependent spectral absorptivities of metallic materials in the infrared, J. Thermophys. Heat Transf. **20**, 9 (2006).
[30] J. Xie and A. Kar, Laser welding of thin sheet steel with surface oxidation, Weld. J. **78**, 343 (1999).
[31] G. S. Arnold, Absorptivity of several metals at 10.6 um: Empirical expressions for the temperature dependence computed from Drude theory, Appl. Opt. **23**, 1434 (1984).
[32] T. Klein, M. Vicanek, G. Kroos, I. Decker, and G. Simon, Oscillations of the keyhole in penetration laser beam welding, J. Phys. D. Appl. Phys. **27**, 2023 (1994).
[33] M. Courtois, M. Carin, P. Le Masson, S. Gaied, and M. Balabane, A new approach to compute multi-reflections of laser beam in a keyhole for heat transfer and fluid flow modelling in laser welding, J. Phys. D. Appl. Phys. **46**, 505305 (2013).
[34] V. Bruyere, C. Touvrey, and P. Namy, in *Proc. 2013 COMSOL Conf.* (2013), pp. 1–7.
[35] J. Y. Lee, S. H. Ko, D. F. Farson, and C. D. Yoo, Mechanism of keyhole formation and stability in stationary laser welding, J. Phys. D. Appl. Phys. **35**, 1570 (2002).
[36] A. Matsunawa, J.-D. Kim, N. Seto, M. Mizutani, and S. Katayama, Dynamics of keyhole and molten pool in laser welding, J. Laser Appl. **10**, 247 (1998).
[37] V. V. Semak, J. A. Hopkins, M. H. McCay, and T. D. McCay, Melt pool dynamics during laser welding, J. Phys. D. Appl. Phys. **28**, 2443 (1995).
[38] J. Wang, C. Wang, X. Meng, X. Hu, Y. Yu, and S. Yu, Study on the periodic oscillation of plasma/vapour induced during high power fibre laser penetration welding, Opt. Laser Technol. **44**, 67 (2012).
[39] T. Klein, M. Vicanek, and G. Simon, Forced oscillations of the keyhole in penetration laser beam welding, J. Phys. D. Appl. Phys. **29**, 322 (1996).
[40] Z. Szymanski, J. Hoffman, and J. Kurzyna, Plasma plume oscillations during welding of thin metal sheets with a CW CO2 laser, J. Phys. D Appl. Phys. **34**, 189 (2001).
[41] L. Mrňa and M. Šarbort, Plasma bursts in deep penetration laser welding, Phys. Procedia **56**, 1261 (2014).
[42] T. Sibillano, A. Ancona, D. Rizzi, V. Lupo, L. Tricarico, and P. M. Lugarà, Plasma plume oscillations monitoring during laser welding of stainless steel by discrete wavelet transform application, Sensors **10**, 3549 (2010).
[43] H. Gu and W. W. Duley, Resonant acoustic emission during laser welding of metals, J. Phys. D. Appl. Phys. **29**, 550 (1996).
[44] D. Farson, K. Hillsley, J. Sames, and R. Young, Frequency–time characteristics of air-borne signals from laser welds, J. Laser Appl. **8**, 33 (1996).
[45] M. Haran, D. P. Hand, S. M. Ebrahim, C. Peters, and J. D. C. Jones, Optical signal oscillations in laser keyhole welding and potential application to lab welding, Meas. Sci. Technol. **8**, 627 (1997).
[46] J. Kroos, U. Gratzke, M. Wcanek, and G. Simon, Dynamic behaviour of the keyhole in laser welding, J. Phys. D. Appl. Phys. **26**, 481 (1993).
[47] Y. H. Xiao and G. Den Ouden, A study of GTA weld pool oscillation, Weld. J. **69**, 289 (1990).
[48] K. C. Mills, Y. Su, Z. Li, and R. F. Brooks, Equations for the calculation of the thermo-physical properties of stainless steel, ISIJ Int. **44**, 1661 (2004).